Ground-Based Passive Microwave Profiling during Dynamic Weather Conditions

K. R. KNUPP,* R. WARE,+,# D. CIMINI,@ F. VANDENBERGHE,# J. VIVEKANANDAN,#
E. WESTWATER,& T. COLEMAN,* AND D. PHILLIPS*

* *University of Alabama in Huntsville, Huntsville, Alabama*
+ *Radiometrics Corporation, Boulder, Colorado*
# *National Center for Atmospheric Research, Boulder, Colorado*
@ *Center of Excellence CETEMPS, University of L'Aquila, Coppito, L'Aquila, Italy*
& *NOAA/CU Center for Environmental Technology, Department of Electrical and Computer Engineering, University of Colorado, Boulder, Colorado*

(Manuscript received 1 April 2008, in final form 5 August 2008)

ABSTRACT

Short-period (1–5 min) temperature and humidity soundings up to 10-km height are retrieved from ground-based 12-channel microwave radiometer profiler (MWRP) observations. In contrast to radiosondes, the radiometric retrievals provide very high temporal resolution (1 min or less) of thermodynamic profiles, but the vertical resolution, which declines in proportion to the height above ground level, is lower. The high temporal resolution is able to resolve detailed meso-γ-scale thermodynamic and limited microphysical features of various rapidly changing mesoscale and/or hazardous weather phenomena. To illustrate the MWRP capabilities and potential benefits to research and operational activities, the authors present example radiometric retrievals from a variety of dynamic weather phenomena including upslope supercooled fog, snowfall, a complex cold front, a nocturnal bore, and a squall line accompanied by a wake low and other rapid variations in low-level water vapor and temperature.

1. Introduction

The thermodynamic state of atmospheric conditions above the surface has been traditionally sampled at synoptic-scale spacing twice daily by radiosondes. However, the temporal and spatial resolution of these soundings does not resolve the temperature and humidity changes associated with most microscale and mesoscale phenomena, which evolve on temporal scales of minutes to hours, and have spatial scales of 1–10 km. The high-frequency sampling of thermodynamic profiles promotes the understanding of complex mesoscale phenomena and is likely a prerequisite to improvements in weather prediction. Although the Geostationary Operational Environmental Satellite (GOES) and polar orbiting satellite infrared sounders have the potential to provide thermodynamic profile measurements (e.g., Chahine et al. 2006; Zhou et al. 2007), they are limited by relatively crude vertical resolution at lower levels within the important atmospheric boundary layer (ABL) and/or by the presence of optically thick clouds. Continuous ground-based radiometric profiler observations can be used to fill the temporal gaps between radiosonde soundings. Although ground-based infrared sounding systems show promise (Feltz et al. 2003), microwave radiometers have a broader capability and can generally provide profiles during cloudy and light-precipitating conditions.

This paper examines the measurement capabilities of a 12-channel microwave radiometer profiler (MWRP). A general description of ground-based radiometric thermodynamic profiling is given in Westwater (1993), and early experimental results from a 6-channel radiometer are discussed in Hogg et al. (1983a). Recent work relevant to both this study and the MWRP includes a general description of the instrument (Ware et al. 2003), thermodynamic profiling capabilities and applications (Güldner and Spänkuch 2001; Liljegren et al. 2005; Cimini et al. 2006), and capabilities to measure cloud/precipitation characteristics (Li et al. 1997; Marzano et al. 2005). A recent and comprehensive

Corresponding author address: K. R. Knupp, Department of Atmospheric Science, University of Alabama in Huntsville, Huntsville, AL 35805.
E-mail: kevin.knupp@nsstc.uah.edu

DOI: 10.1175/2008JTECHA1150.1

TABLE 1. Definition of symbols corresponding to MWRP retrieved parameters, or derivatives of these parameters.

Symbol	Definition
T	Retrieved temperature
T_{IR}	Infrared temperature
ρ_v	Retrieved water vapor density
ρ_L	Retrieved liquid water density
RH	Retrieved RH
IWV	Retrieved integrated water vapor
ICW	Retrieved integrated cloud water
θ	Potential temperature (derived from T)
r_v	Water vapor mixing ratio (derived from ρ_v)

review of radiometers and their physical principles is given in Westwater et al. (2005).

In this paper, we focus on the MWRP's capability to resolve rapidly changing thermodynamic profiles within a wide variety of mesoscale weather systems, including upslope supercooled fog and snowfall at Boulder, Colorado, and a bore, complex cold front and intense squall line from Huntsville, Alabama.

2. Radiometer characteristics and other data

a. Radiometer characteristics

The Radiometrics 12-channel MWRP observes atmospheric brightness temperatures in five frequency bands from 22 to 30 GHz, and in seven bands from 51 to 59 GHz. A separate infrared radiometer receives downwelling IR radiation in the 9.6–11.5-μm band, which is converted to a zenith infrared temperature (T_{IR}) of cloud base. In situ surface temperature, humidity, and pressure sensors provide surface conditions. The radiometer has automated elevation and (an optional) azimuth scanning capability, and the observation interval in the current instruments can be as short as 10 s. The antenna beamwidth ranges from 2° at 59 GHz to 6° at 22 GHz. The instrument is portable, with 0.12-m^3 volume and 32-kg weight. Additional details can be found in Solheim et al. (1998) and Ware et al. (2003).

Profiles of temperature (T), water vapor density (ρ_v), and liquid water density (ρ_L) are retrieved using neural networks trained with several years of historical radiosonde soundings from a location with similar altitude and climatology to the radiometer site. Hereafter, the symbols defined in Table 1 will be used. Profiles of ρ_L are artificially added to the radiosonde soundings when an RH value exceeds a threshold, typically 93%. Radiosonde profiles are forward modeled using radiative transfer equations (Schroeder and Westwater 1991) to estimate the microwave brightness temperature spectrum incident at ground level for each sounding. Neural network inputs include microwave brightness temperatures from the 12 channels; surface temperature, relative humidity, and pressure; and cloud-base temperature. Neural network outputs include T, ρ_v, RH, and ρ_L profiles at 47 heights from ground level to 10 km AGL, and integrated water vapor (IWV) and integrated cloud water (ICW). The neural network retrieval method is described by Solheim et al. (1998).

Errors typically assigned to radiosonde data, when assimilated into numerical weather models, are shown in Fig. 1. *Representativeness* error resulting from the characterization of a model cell volume by the radiosonde point measurement is dominant. Also shown in Fig. 1 are radiometric retrieval errors determined from statistical comparisons with radiosondes at midlatitude and arctic sites (Güldner and Spänkuch 2001; Liljegren et al. 2001). The radiometric retrievals are based on volumetric (time integrated) measurements at zenith, and are also susceptible to representativeness error, but at a reduced level compared to the radiosonde soundings. (The radiosonde represents a nonsimultaneous moving point measurement, not a time-integrated vertical profile.) For T retrievals, the radiometer statistical comparison RMS is smaller than the radiosonde representativeness error in the boundary layer and is slightly higher above the boundary layer, reaching a maximum of 2.1 K at 7-km height. The radiometer ρ_v retrieval statistical comparison RMS shows a maximum of 1 g m^{-3} at 2 km AGL, and is smaller than radiosonde representativeness error at all heights. The effective resolution of the MWRP is highest near ground level and gradually decreases with height (Cimini et al. 2006). In general, cotemporal radiometer and radiosonde soundings are of comparable accuracy when used to characterize atmospheric volumes in numerical weather models (Westwater et al. 2000; Güldner and Spänkuch 2001; Ware et al. 2003).

The accuracy of liquid profiles retrieved from the MWRP has been difficult to determine because of inherent differences in fixed volume radiometer sensing and variable temporal and spatial sampling of aircraft point measurements or special radiosonde supercooled liquid sensors. However, a 50% agreement between zenith MWRP supercooled liquid profiles and special radiosonde measurements along uncontrolled flight paths was reported by Ware et al. (2003). The accuracy of the IWV measurement using the dual-channel technique (around 22 and 31 GHz) is about 1 mm (Hogg et al. 1983b; Han and Westwater 1995). Likewise, the accuracy of ICW is estimated at 10%–20% (Westwater 1993).

For the Boulder examples, MWRP measurements were acquired at 5-min intervals, while the Huntsville radiometer sampled with a 1-min period. Thermodynamic

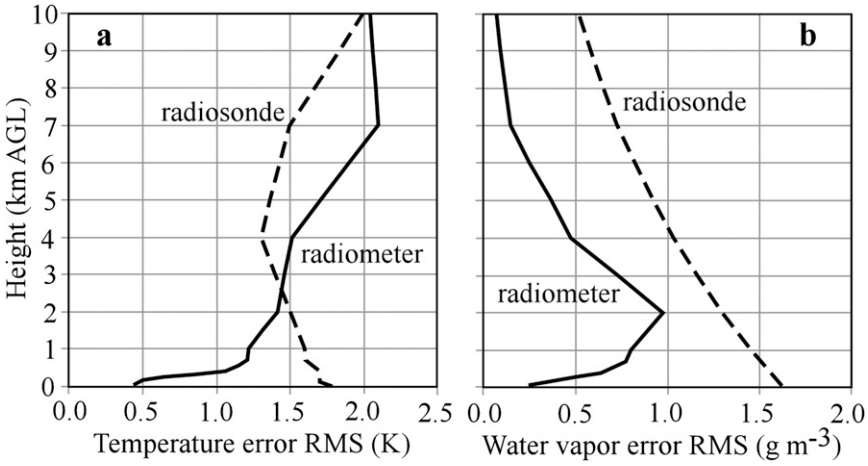

FIG. 1. Radiometric retrieval accuracy for (a) temperature and (b) water vapor density determined by comparison with radiosondes for all seasons. Radiosonde errors are those typically assigned by NCEP when radiosonde data are used in numerical weather modeling. Statistics of radiometric retrieval comparisons with radiosonde soundings are taken from Güldner and Spänkuch (2001) and Liljegren et al. (2001).

retrievals at both locations were obtained using the same neural network algorithm.

b. Measurements from Huntsville

The University of Alabama in Huntsville (UAH) maintains a cluster of profiling instruments, including an MWRP of the type described in the previous subsection. The T and ρ_v retrievals were transformed to potential temperature (θ) and water vapor mixing ratio (r_v), both of which are conserved for subsaturated adiabatic motions. Other instruments include a 915-MHz Doppler wind profiler, a 2-kHz Doppler sodar, a lidar ceilometer (0.905 μm), and surface instrumentation, all located at the UAH profiling site on campus. When in mobile form, these instruments compose the UAH Mobile Integrated Profiling System (MIPS; see http://vortex.nsstc.uah.edu/mips/ for details). A GPS radiosonde system is located on Redstone Arsenal (RSA), 14 km to the south.

3. Measurements

The diversity of radiometric measurements is illustrated with five contrasting examples presented in the following subsections. These cases include measurements from an upslope supercooled fog event and snow event in Boulder, and a bore, complex cold front and squall line in Huntsville. The appendix (Fig. A1) provides surface and 500-hPa analyses for each case.

a. Upslope with supercooled fog

Prolonged upslope weather conditions occurred in the Denver (DEN) area from 14 to 17 February 2001. An initial cold front passed over the MWRP on 14 February. A secondary surge of cold air associated with a larger, colder, and more intense trailing anticyclone reinforced the upslope flow around Denver on 16–17 February (Fig. A1a). Radiometric retrievals up to 2 km AGL (ground level is about 1.6 km MSL at Boulder) on 16 February 2001 are shown in Fig. 2. Advection of cold air behind the secondary cold frontal surge produced shallow moist upslope (easterly) flow along the Front Range, beginning near 1045 UTC 16 February. The passage of this shallow front is represented as a modest 3°C decrease in surface temperature (Fig. 3a) and a 15% increase in surface RH (Fig. 3a) during the 1-h period following the frontal passage. Figures 2a and 2b clearly show that the frontal passage was confined to levels below about 500 m AGL, where the cold, moist air is most prominent.

Clear conditions prior to and just after the frontal passage were followed by a rapid onset of fog at 1140 UTC, as indicated by the step increase in T_{IR} to 265 K by 1150 UTC (Fig. 3b). ICW values (Fig. 3d) reached a maximum of 0.26 mm near 1715 UTC. The corresponding maximum value of retrieved ρ_L was around 0.6 g m^{-3} at 300 m AGL when the depth of the cold, moist air was near a maximum. The presence of fog is substantiated by the near equality in T_{IR} and actual air temperature, both measured at about 265 K. Thus, the 500-m-deep fog layer was supercooled, with a mean temperature of about −8°C. The IWV retrieval (Fig. 3c) shows a steady increase from 5.1 mm at the time of frontal passage to 6.5 mm near 2000 UTC. The radiometer rain sensor (not shown) did not indicate wetting from liquid precipitation accumulation during this period.

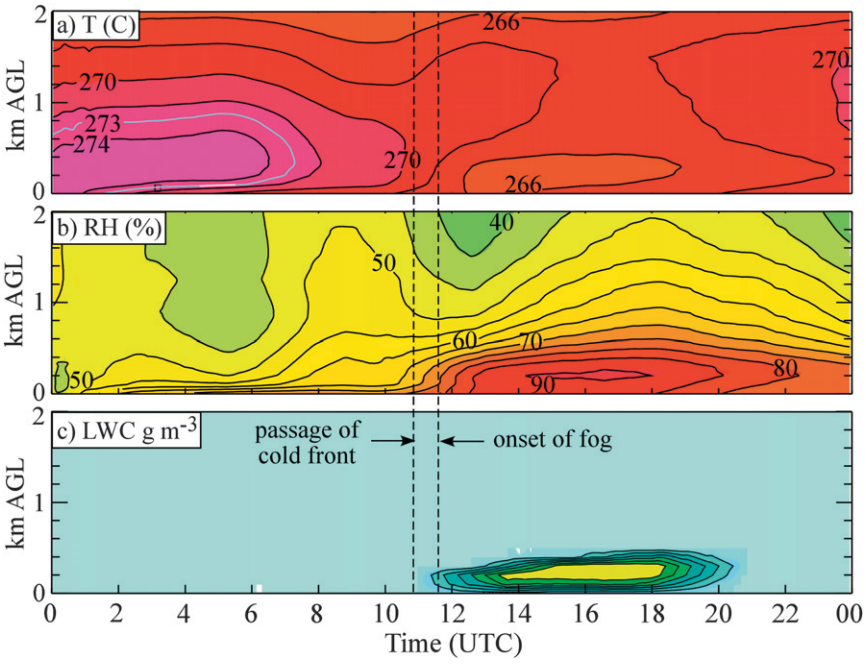

FIG. 2. Radiometric retrievals (plotted in time–height format) of (a) T (K), (b) RH (%), and (c) LWC (drawn at 0.1 g m^{-3} intervals starting at 0.1 g m^{-3}) during a supercooled fog event associated with upslope flow at Boulder on 16 Feb 2001. The vertical dashed lines indicate the time of frontal passage and subsequent fog arrival over the radiometer.

A comparison of the radiometer sounding with the 1200 UTC 16 February 2001 radiosonde sounding at Denver (located 50 km southeast of Boulder) is shown in Fig. 4. A deep temperature inversion extends from 400 to 900 m AGL, high RH exists below 500 m, and a tropopause height near 10 km is indicated in both the radiosonde and radiometer soundings. The retrieved fog/stratus ρ_L maximum value of 0.14 g m^{-3} (inset in Fig. 4) located near 300 m AGL is consistent with observations of fog at this time (e.g., Gerber et al. 1999).

Poor visibility and icing conditions during this upslope event led to major disruptions in surface and air transportation in the Denver area, including the diversion of flights from Denver International Airport for 18 h. Fog was not predicted by numerical forecasts that used the Denver radiosonde. However, in a retrospective study with the fifth-generation Pennsylvania State University–National Center for Atmospheric Research Mesoscale Model (MM5) adjoint model, it was possible to reproduce the fog in the Boulder–Denver area through assimilation of the Boulder radiometric retrievals (Vandenberghe and Ware 2003).

Eleven hours prior to the fog, the 0000 UTC 16 February Boulder radiometric retrieval (Fig. 2) and Denver radiosonde sounding (not shown) showed RH less than 45% below 500-m height. During the following 11 h, the 5-min retrieved RH increased slowly prior to the rapid increase to >90% following the cold frontal passage at 1045 UTC. A similar trend was observed in Boulder prior to another similar event that produced supercooled fog, freezing drizzle, and snow on 4 March 2003. Radiometric retrievals, weather radar, cloud radar, lidar, and tower observations during this weather event are described in Herzegh et al. (2003) and Ikeda and Rasmussen (2003). The high-resolution radiometer measurements in both cases suggest that trends in RH can be used to more accurately predict the onset of fog. Increased skill is expected if raw radiometric brightness temperatures (rather than retrieved profiles) are directly assimilated into numerical weather models (Nehrkorn and Grassotti 2003).

b. Snowfall

Radiometric retrievals during a light snowfall event associated with weak upslope flow (Fig. A1b) in Boulder on 23 December 2002 are shown over the lowest 3 km AGL in Fig. 5. Relatively dry (low density) snow that sublimated several minutes after touching the ground was visually observed at the radiometer site. Retrieved T profiles up to 3 km AGL (Fig. 5a) are less than 270 K and show a gradual warming below 500 m AGL from 1600 to 2100 UTC, followed by a cooling trend. RH (with respect to water—not ice—saturation; Fig. 5b) exceeds 90% between 0.5 and 2 km AGL

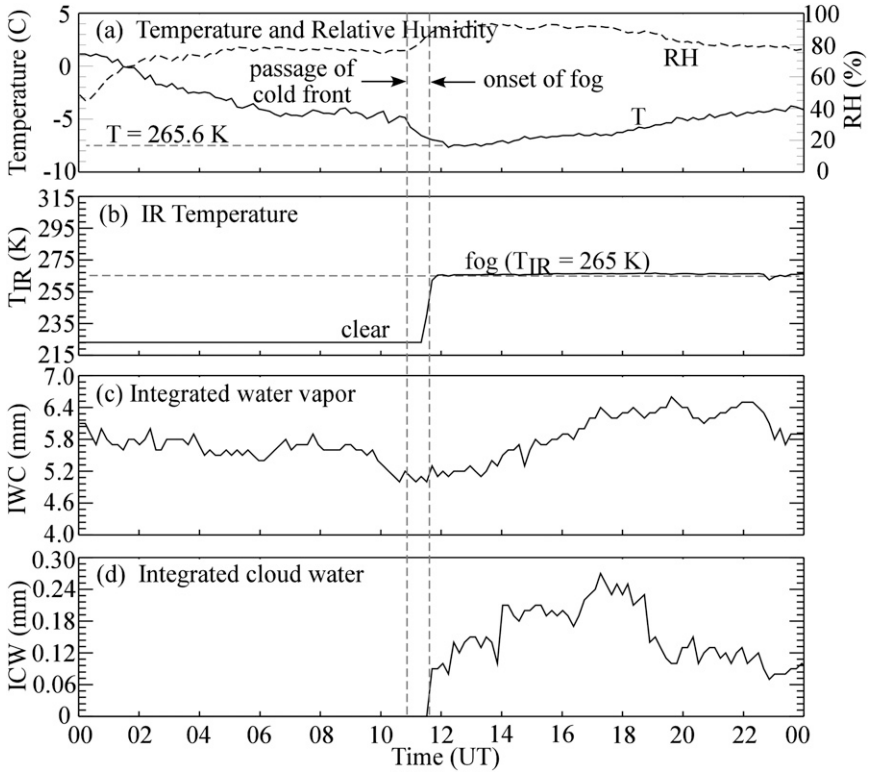

FIG. 3. Surface time series derived from radiometer measurements: (a) T and RH, (b) T_{IR}, (c) IVW, and (d) ICW for the same time period as in Fig. 2. The frontal passage and fog arrival times are indicated by the vertical dashed lines.

during most of the observation period. A ρ_L value of about 0.1 g m^{-3} magnitude is shown between 0.5 and 1.2 km AGL from 2050 to 2210 UTC in Fig. 5c.

Figures 5c and 6b,d indicate a continuous cloud layer with a cloud-base temperature (T_{IR}) of 264 K between 1900 and 2300 UTC. During this period the surface temperature was around 271 K, the IWV fluctuated around 6.6 mm, and ICW exhibited peak values that oscillated between 0.14 and 0.34 mm between 2030 and 2215 UTC. The snow that formed during this period would have likely exhibited some riming within this layer of supercooled water.

The Denver radiosonde sounding at 0000 UTC 24 December 2002 and the Boulder radiometer sounding at 2354 UTC 23 December 2002 are shown in Fig. 7. The radiometric T retrieval is 2–3 K warmer than the radiosonde sounding from 1 to 3 km AGL, and is ~8 K warmer at the tropopause. The radiosonde RH measurement increases from 65% at the surface to 80% at 700 m AGL and then remains above 75% up to 4.5 km. The retrieved radiometer RH increases from 80% at the surface to near saturation at 0.9 km (close to the cloud-base temperature of 264 K) and remains close to saturation to 1.75 km AGL. These T and RH differences between DEN and the radiometer may be attributed to sampling differences (Lagrangian point sampling for the radiosonde and fixed volume measurements for the radiometer), to the vertical resolution characteristics of the instruments, and to atmospheric variability over the 50-km distance between the two measurement locations.

During the 11 h prior to snowfall, RH at 1 km AGL steadily increased from 50% to 100%. Since saturation is required for cloud and precipitation formation, trends in the RH profile could potentially improve local short-term cloud and precipitation forecasting.

c. *Bores and gravity wave phenomena*

Bores and gravity wave phenomena are relatively common, but their detailed thermodynamic structure has been difficult to measure because of their relatively short period and wavelength. Bores are hydraulic jumps that are often triggered by a density current (gust front) or cold front intruding into a stable air mass near the surface (Simpson 1997). They are typically associated with a low-level wind shift in the direction of bore motion and a permanent upward displacement of the low-level air mass. A recent study by Knupp (2006)

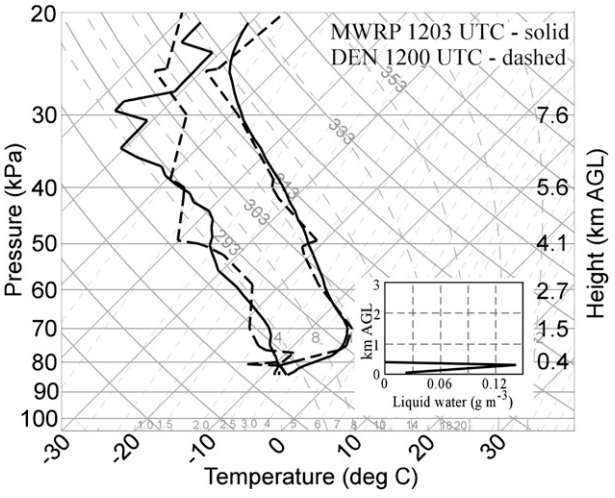

FIG. 4. Skew T–log$p$ plots of T and T_d retrieved from the MWRP at Boulder (solid) and the National Weather Service radiosonde sounding from Denver at 1200 UTC 16 Feb 2001 (dashed). Both soundings indicate a surface-based inversion up to 1 km AGL and low dewpoint depression (high RH) up to 300 m AGL. The radiometric ρ_L (inset, lower right, matched to the skew T–log$p$ pressure levels) shows a maximum ρ_L of 0.14 g m^{-3} near 300 m AGL.

utilized the MWRP (with only 14-min temporal resolution) and other MIPS instruments to examine a bore passage in Oklahoma. In this section, 1-min measurements of a ''typical'' bore are presented to illustrate the thermodynamic properties of bores at much higher temporal resolution.

On 16 May 2007 a well-formed bore was sampled around 0500 UTC (2330 LST) in advance of a weakening mesoscale convective system (MCS) and cold front (Fig. A1c). During the bore passage, the surface T decreased by 2°–3°C, and the dewpoint increased more slowly by about the same magnitude (Fig. 8a). A distinct wind shift from 200° to 250° was recorded from the surface (Fig. 8b) up to about 0.8 km AGL, and a relative maximum in surface wind (gust to 7 m s^{-1}; Fig. 8c) was followed by wind speeds <2 m s^{-1}. The absence of a feeder flow[1] (as indicated by the surface ground–relative wind speed decrease to 1–2 m s^{-1} following the bore passage) and the prolonged increase in surface pressure of about 1 hPa (relative to the background trend indicated in Fig. 8d) are characteristic surface signatures of bores (e.g., Koch et al. 1991; Knupp 2006).

The MWRP analysis in Figs. 9a and 9b shows a well-defined reduction in θ (i.e., a rise in the isentropes) over the lowest 1.2 km, and a significant increase in r_v over a deeper layer due to the upward displacement of air within the bore, and horizontal advection following the bore, at low levels. The hydrostatic pressure increase associated with the observed average cooling of about 2 K over the lowest 1200 m is about 0.9 hPa, which duplicates the measured surface pressure increase during the bore passage.

Data from the 915-MHz wind profiler (not shown) indicated an updraft of 1–2 m s^{-1} over the lowest 1.5 km. The 915-MHz signal-to-noise ratio (SNR) patterns suggest that a cumulus cloud extended to 3.8 km AGL within the summit of this updraft located above the bore front. The ceilometer (Fig. 9c) recorded a cloud base near 1.5 km AGL within this updraft, and mostly thin clouds[2] persisted near the 1.7-km-AGL level following the bore passage. Indeed, the MWRP integrated cloud water value of 1.6 mm (Fig. 8g) measured at 0508 UTC is consistent with a cloud of 2.3-km depth, as suggested by the 915-MHz SNR (not shown).

Since both θ and r_v are conserved (for subsaturated adiabatic motion), the upward displacements of the isentropes and isohumes provide an estimate of the upward displacement distance of air parcels in this case. The 299-K isentrope (highlighted dashed line in Fig. 9a) ascended 0.8 km, while the 9 g kg^{-1} isohume rose about 0.9 km. The enhanced aerosol backscatter within the residual layer (Fig. 9c) shows a rise that is nearly simultaneous with that of the θ and r_v contours. While the isentropes assumed a horizontal orientation following the initial bore passage, the isohumes exhibit an undulation in time. This latter pattern suggests that waves were present in the wake of the bore, an observation that suggests this was an undular bore (Clarke et al. 1981). The moistening of the lower atmosphere associated with the bore passage was significant in this case, as values of IWV increased by about 6 mm, or 20% (Fig. 8f). Moreover, the lifting associated with the bore destabilized the lowest 0.4 km, based on analysis of Brunt–Väisälä frequency computed from retrieved MWRP temperature profiles.

d. *Finescale structure of a cold front*

MWRP observations of cold fronts, gust fronts, and other boundaries often disclose finescale structures that have enhanced understanding of these types of

[1] A feeder flow in a gravity current is defined as a flow that moves at least as fast as the gravity current head (gust front), that is, there is relative flow from rear to front.

[2] The thin clouds are inferred from low (below noise) values of ICW in the presence of uniform cloud-base height measured by the ceilometer.

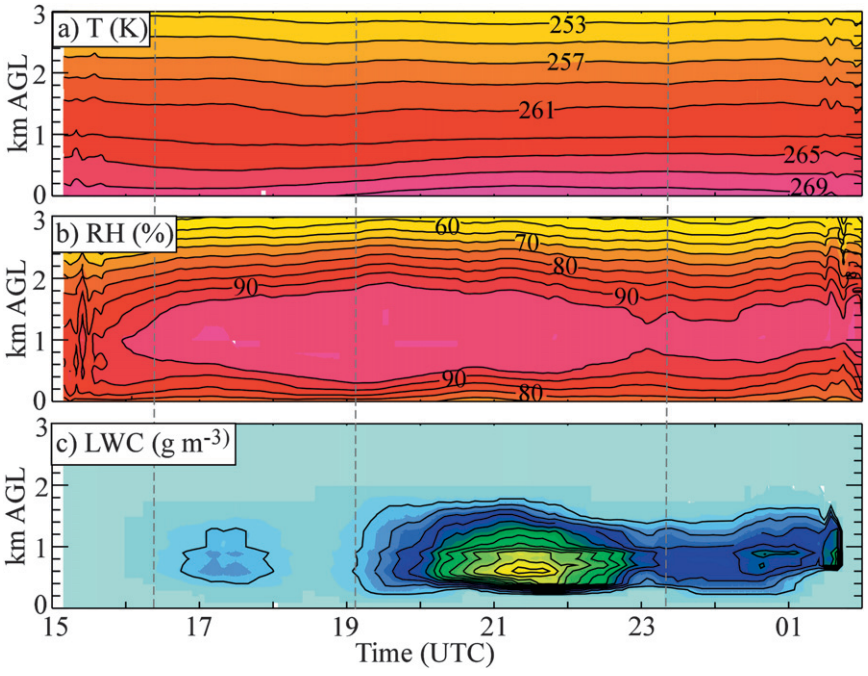

FIG. 5. As in Fig. 2, but for 23 Dec 2002. RH is near saturation around 1 km AGL, and corresponds to low values of retrieved LCW, drawn at 0.02 g m^{-3} intervals starting at 0.02 g m^{-3}.

phenomena. For example, Karan and Knupp (2006) described profiler observations [collected during the International H_2O Project (IHOP)] of several boundary types.

On 16 March 2007 a relatively strong and complex cold front was sampled by the MIPS. This front was associated with a surface cyclone and significant trough at 500 hPa (Fig. A1d). Figure 10 shows the MWRP θ and r_v retrievals along with the 915-MHz SNR around the time of the frontal passage. Corresponding surface time series are presented in Fig. 11. Five

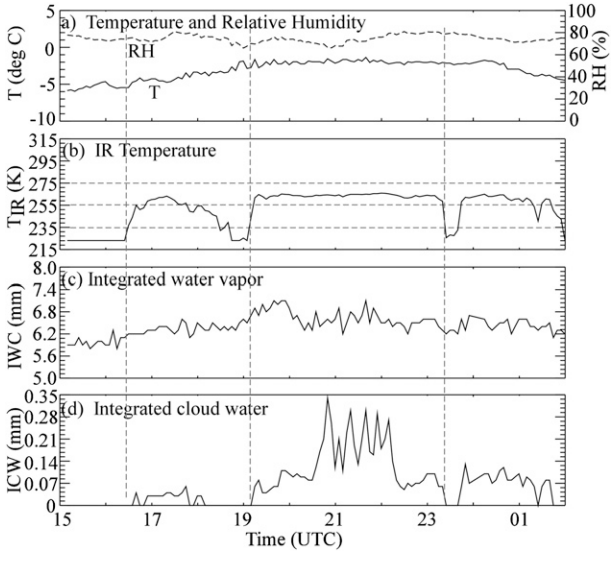

FIG. 6. As in Fig. 3, but for 23 Dec 2002. Vertical dashed lines mark the distinct cloud borders referred to in the text.

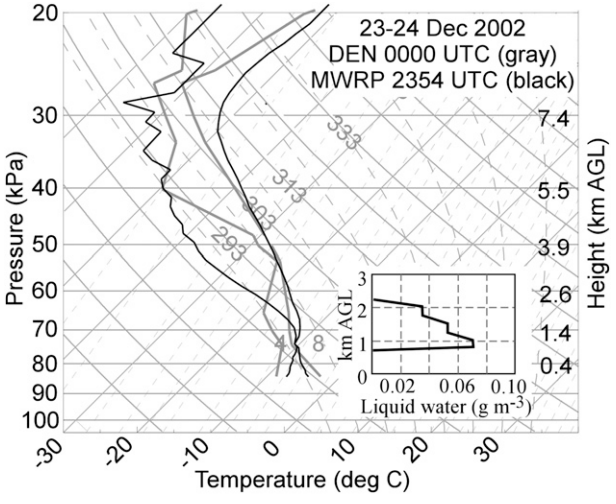

FIG. 7. MWRP retrieved sounding (black) and Denver radiosonde (gray) for a light snowfall event at Boulder on 23 Dec 2002. The MWRP sounding shows RH saturation from 1- to 2-km height and 0.07 g m^{-3} equivalent liquid density (inset, lower right, matched to the skew T–log$p$ pressure levels) near 1-km height.

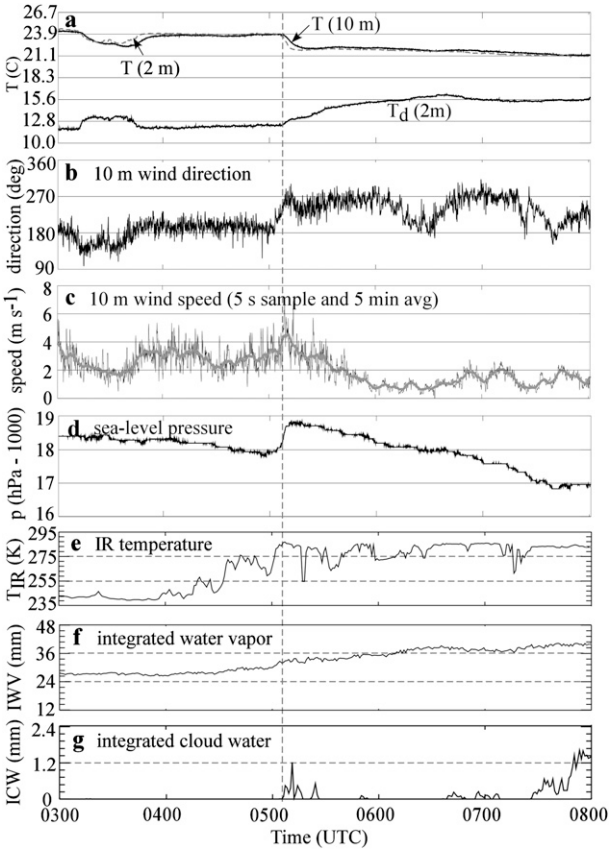

FIG. 8. Time series of surface parameters (derived from independent surface instrumentation) and MWRP data from the bore case of 16 May 2007. Surface parameters include (a) T and T_d (°C), (b) 10-m wind direction, (c) 10-m wind speed, and (d) pressure (reduced to sea level). MWRP parameters include (e) T_{IR} temperature, (f) IWV, and (g) ICW. The vertical dashed line represents the bore passage.

thermodynamic transitions (labeled 1–5 in Figs. 10 and 11) are identified by the vertical dashed lines. The first boundary was associated with rainfall evaporation near the leading edge of the frontal rainband identified in Fig. 10c. It is marked by surface cooling of ~2 K and a surface wind shift to 4 m s^{-1} northerly flow below 0.5 km AGL. This feature resembles a shallow density current, a common feature of squall lines.

More appreciable cooling and drying were associated with the surface passage of the cold front, identified as the vertical dashed line labeled "2." This frontal feature was marked by an increase in northerly winds to 6 m s^{-1} (10 m s^{-1} aloft), a second distinct temperature break at the surface, and a modest pressure increase of 1 hPa (Figs. 11a,b). While the MWRP retrieved θ indicates that cooling was most substantial below 1 km AGL, cooling did extend to 3–4 km AGL, and is corroborated by the lowering of the brightband level shown in Fig. 10c.

The passage of a second cold frontal gradient (labeled 3) near 0840 UTC is most evident in (i) the r_v field above 0.6 km AGL (Fig. 10b), (ii) the θ field (a secondary cold surge) between 0.5 and 1.5 km AGL (Fig. 10a), and (iii) a significant reduction in IWV (Fig. 11f). This feature was associated with an increase in 915-MHz SNR (backscatter), which may have been produced by mixing, and therefore enhanced Bragg scattering, within this frontal zone. Normally, such a signature indicates the presence of cloud, but in this case the retrieved ICW was near zero, suggesting that appreciable clouds were absent within the 1–3-km-AGL layer. The slope of this SNR feature is consistent with the slope of the enhanced gradient in the retrieved r_v field. At the surface, the only significant surface feature was a 1.5-mb pressure increase; changes in thermodynamic variables were insignificant.

A third frontal gradient (labeled as 4) is represented by significant cold air advection beginning near 1040 UTC between 0.5 and 4.0 km AGL. Again, the surface thermodynamic signature is very subtle, but a significant and sustained pressure rise marked the onset of this deep layer of cold advection aloft. Such a pressure increase is more typically associated with the arrival of cold air at the surface.

The fourth and final frontal gradient (labeled 5) occurred just after 1500 UTC and is represented by the onset of advection of drier air and a secondary surge of cold air above 1.0 km AGL. The corresponding surface signatures include a modest drop in dewpoint and a secondary pressure surge.

During passage of the four cold frontal segments, the low-level atmosphere remained close to saturation, and hence the stratocumulus cloud base, as measured by the ceilometer (not shown), remained near 100–200 m AGL during the 0400–1400 UTC time period. However, T_{IR} measurements (Fig. 11d) display a slow decrease that is commensurate with the decrease in surface T and T_d. The time series of ICW in Fig. 11f reveals the prefrontal rainband passage between 0500 and 0600 UTC, two shallow postfrontal showers near 0700 UTC, and a shallow drizzle shower (~1 km deep, as indicated by the 915-MHz profiler and annotated in Fig. 10c) that corresponds to the relative maximum in ICW near 1300 UTC.

A comparison of the postfrontal MWRP sounding with the RSA radiosonde (located 14 km to the south) at 1117 and 1141 UTC, respectively, is displayed in Fig. 12. The MWRP sounding is 1500 s earlier than the RSA balloon sounding to account for temperature advection based on the observed 10 m s^{-1} northerly postfrontal wind. Cloud base and top are located near 985 and 900 hPa, respectively. Although the MWRP did not fully

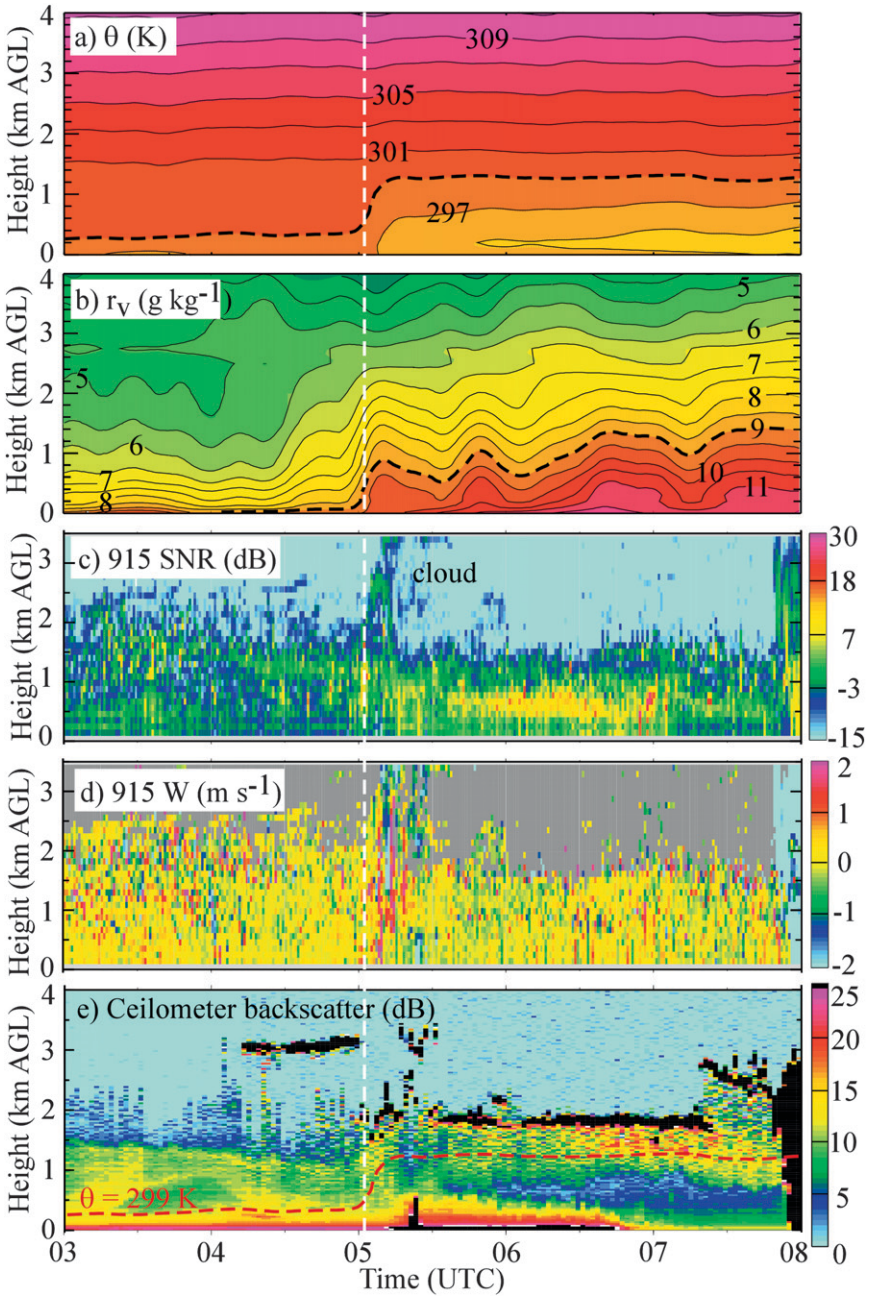

FIG. 9. Time vs height sections of parameters illustrating the passage of a bore on 16 May 2007. (a) MWRP-derived θ, contoured every 2 K (the 299-K isentrope is dashed), (b) MWRP-derived mixing ratio, contoured every 0.5 g kg^{-1} (the 9 g kg^{-1} isohume is dashed), (c) 915-MHz profiler backscatter, expressed as an SNR, (d) 915-MHz profiler radial velocity from the vertical beam, and (e) range normalized ceilometer backscatter (black shading exceeds values on the scale to the right). The 299-K isentrope from (a) is drawn as the red dashed line in (c). The vertical dashed line represents the bore passage.

resolve the sharp frontal temperature inversion near 880 hPa (about 2 km AGL) and the warm air between 870 and 680 hPa, the relative profile shape is approximately retrieved. In this case, utilization of the 915-MHz profiler, which measured a relative maximum in SNR within the inversion layer near 1 km AGL, indicated by the dashed line in Figs. 10a,c, could have improved the MWRP retrievals using techniques outlined in Gossard

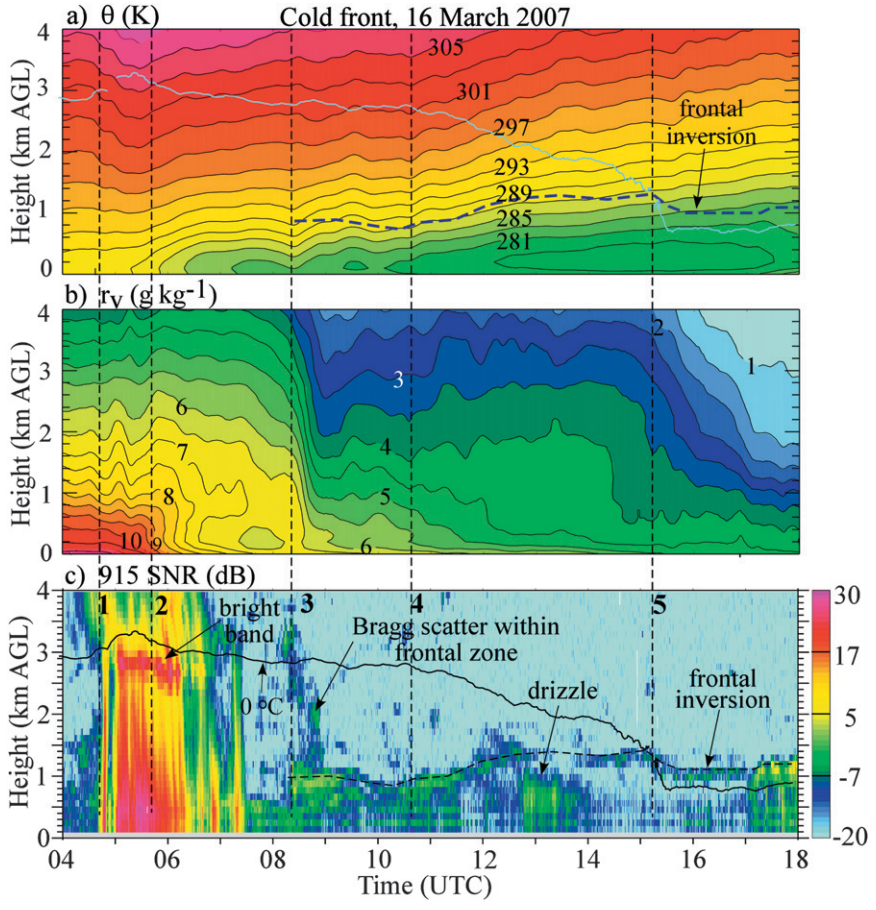

FIG. 10. Time vs height sections of parameters illustrating the passage of a cold frontal system on 16 Mar 2007. (a) MWRP-derived θ, contoured every 2 K, (b) MWRP-derived mixing ratio, contoured every 0.5 g kg^{-1}, and (c) 915-MHz backscatter expressed in an SNR (dB). Vertical lines labeled 1–5 refer to frontal features that are defined in the text. The frontal inversion, inferred from the 915-MHz SNR, is shown as a dashed line in (c), and is overdrawn on the isentropes in (a). The solid black line in (c) represents the 0°C isotherm from the MWRP retrieval. The warm bias produced by precipitation scattering and emission is represented by the upward protrusion of the isotherm above the bright band in (c) (between dashed lines 1 and 2).

et al. (1999), Löhnert et al. (2004), Bianco et al. (2005), and Klaus et al. (2006).

In summary, this cold front exhibited a complex structure consisting of four (five including the initial density current produced by rainfall evaporation) concentrated gradients in θ and/or r_v that were detected by the MWRP. The surface thermodynamic and wind measurements sampled only the density current and initial cold frontal boundary. This case demonstrates that the MWRP is an ideal instrument to study the characteristics of fronts—in particular elevated fronts or secondary frontal transition zones (e.g., cold fronts aloft; see Koch 2001; Locatelli et al. 2002; Schultz 2005). Such finescale frontal structures have not been well resolved in previous studies.

e. Rapid water vapor variations around deep convection

The Huntsville MWRP observations commonly reveal rapidly changing water vapor profiles around deep convection, mesoscale convective systems, and squall lines. MWRP and surface observations of a relatively intense squall line on 8 June 2007 are shown in Figs. 13 and 14 . This squall line formed in advance of an approaching cold front (Fig. A1e). The passage of the squall line near 2100 UTC was accompanied by a wind gust (10 m AGL) to 16 m s^{-1} (not shown), a surface temperature reduction of 11°C, a peak rainfall rate of 150 mm h^{-1}, and a large pressure oscillation between the mesohigh within the convective

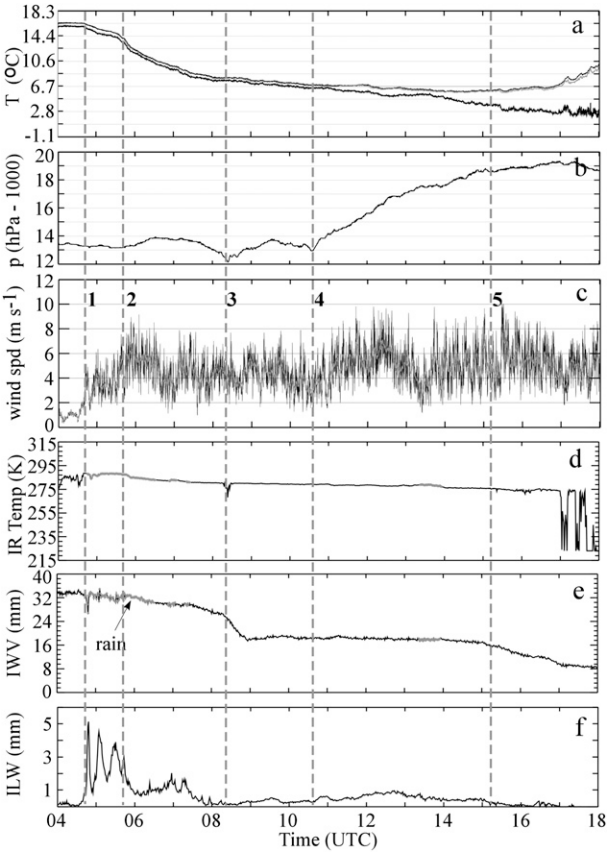

FIG. 11. Time series of surface data (derived from independent surface instrumentation) and MWRP data from the cold frontal system on 16 Mar 2007. Surface parameters include (a) T and T_d, (b) pressure (reduced to sea level), and (c) 10-m wind speed. MWRP parameters include (d) T_{IR}, (e) IWV, and (f) ICW. The vertical dashed lines depict frontal gradients identified in Fig. 10.

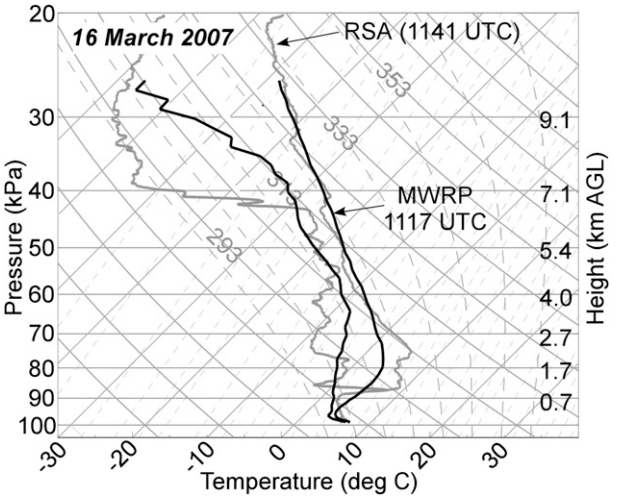

FIG. 12. MWRP and RSA soundings (16 Mar 2007 cold front) plotted on a skew T–log$p$ diagram.

region and a mesolow located within the trailing anvil region.

This case illustrates modest temporal variability in r_v preceding the squall line, and also presents measurements on the thermodynamics of the squall-line density current (cold pool) and the trailing warm ''wake low'' sometimes observed at the rear of squall lines (Johnson 2001). We focus on the variability in r_v for a 24-h period from 0600 UTC 8 June to 0600 UTC 9 June 2007. The step increase in r_v (Fig. 13b) over the lowest 2 km around 0900 UTC is commonly associated with atmospheric bores (section 3c), which appears to be the case here. The passage of a more prominent bore 6 h earlier at 0300 UTC (not shown) produced a similar enhancement in r_v. Following the enhancement in r_v at 0900 UTC, the r_v field remained relatively steady until rapid fluctuations associated with weak showers (about 5 km deep) were recorded near 1740 UTC. Variations in θ and r_v coincide with a surface pressure fluctuation (Fig. 13b), which suggests this feature was an internal gravity wave. A second increase in r_v was recorded after 0300 UTC 9 June, well after the squall-line passage.

A relative minimum in low-level r_v during the 1800–2000 UTC period preceded a significant r_v increase immediately in advance of the squall line, whose gust front and convective core were sampled near 2100 UTC. Two MWRP soundings at 2002 and 2032 (Fig. 15) reveal an appreciable increase in low-level r_v values that raised the mixed layer CAPE (surface to 10 km AGL) from 1200 to 1700 J kg^{-1} (a 42% increase), just before the arrival of the gust front at 2035 UTC.

The gust front and trailing density current annotated in Fig. 13a were well sampled by the MWRP. The top of the cold air, approximated by the bold 301-K isentrope, exhibits a variable height (less than 1 km AGL) following the initial gust front passage at 2045 UTC (see also Fig. 14a). Figures 13a and 13b show a high-amplitude wave in both the θ and r_v contours. Prolonged downward motion (ice terminal fall speed plus subsidence) of 1–2 m s^{-1} was measured between 2200 and 2300 by the 915-MHz wind profiler (Fig. 13d). The surface pressure variation (Fig. 14b) during this wave cycle exhibited a 2-h period and a total variation of 4.5 hPa from the maximum pressure at 2120 to the minimum pressure at 2300 UTC. This low pressure is hydrostatically consistent with the presence of warm air aloft. A comparison of MWRP soundings at 2032 and 2302 (not shown) indicates that warming of 1°–3°C and drying (r_v deficit of -4 g kg^{-1}) between 930 and 600 hPa accompanied the subsidence. Although wake lows have been observed frequently at the rear of squall lines with

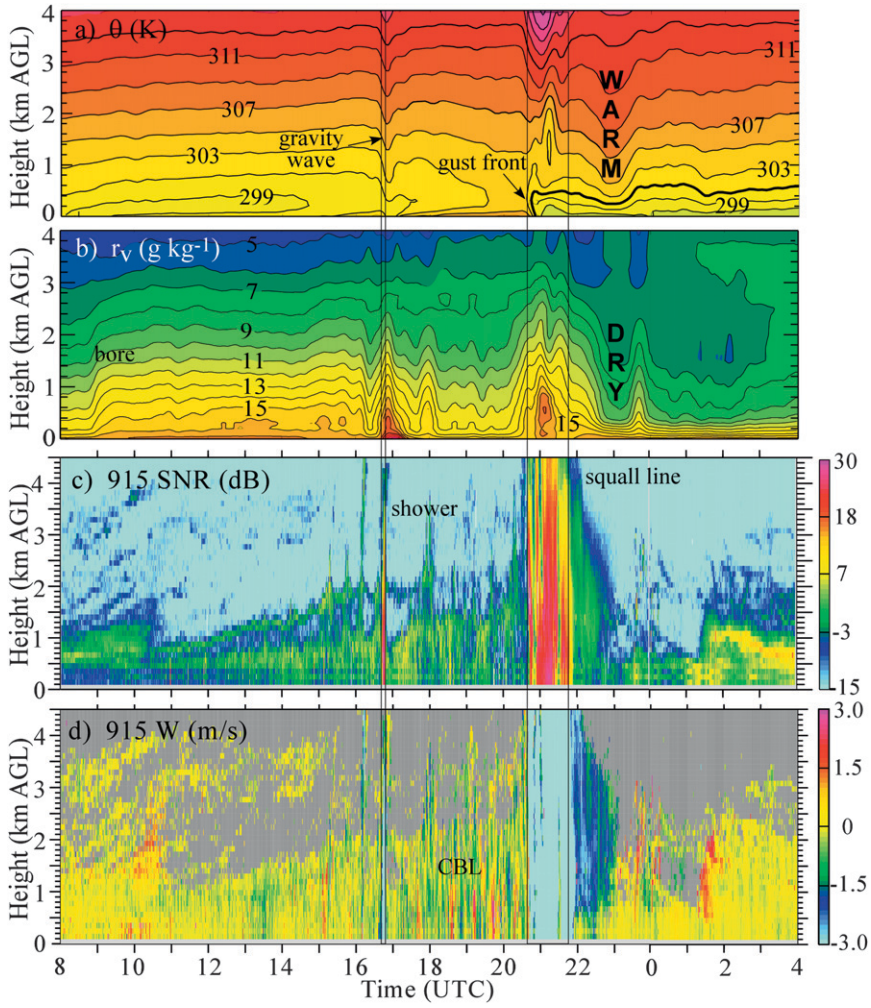

FIG. 13. Time vs height sections of parameters illustrating the prestorm environment and the passage of a squall line on 8 Jun 2007. (a) MWRP-derived θ, contoured every 2 K, (b) MWRP-derived mixing ratio, contoured every 1.0 g kg^{-1}, (c) 915-MHz backscatter expressed in an SNR (dB), and (d) 915-MHz radial velocity from the vertical beam. The warm bias produced by precipitation scattering and emission is present in (a) and (b) (between vertical lines), but the low-level θ appears to have experienced much lower bias. The 301-K isotherm is bold in (a) to identify the low-level density current.

surface data (Loehrer and Johnson 1995) and have been reproduced with a linear model (e.g., Haertel and Johnson 2000), the MWRP observations shown here represent their thermodynamic structure in far greater temporal detail than derived from balloon soundings in previous studies.

4. Discussion and summary

The examples presented in section 3 reveal that MWRP data, combined with data from other ground-based remote sensing instruments such as Doppler radars, UHF wind profilers, acoustic profilers, and lidars, offer considerable scientific insight into complex mesoscale, cloud, and boundary layer processes. Because current MWRP systems provide soundings of T, ρ_v, and ρ_L, along with IWC and ICW every 10–60 s, rapid changes can be resolved, particularly over the lowest 2–3 km AGL where the MWRP retrievals are most accurate. Some benefits to meteorological research and forecasting are summarized in the following text.

a. Boundaries

Sections 3c and 3d establish that the MWRP can provide considerable detail on the rapidly changing thermodynamic structure of translating boundaries such as cold fronts, gust fronts, bores, and gravity waves. The passage of boundaries is associated with thermodynamic

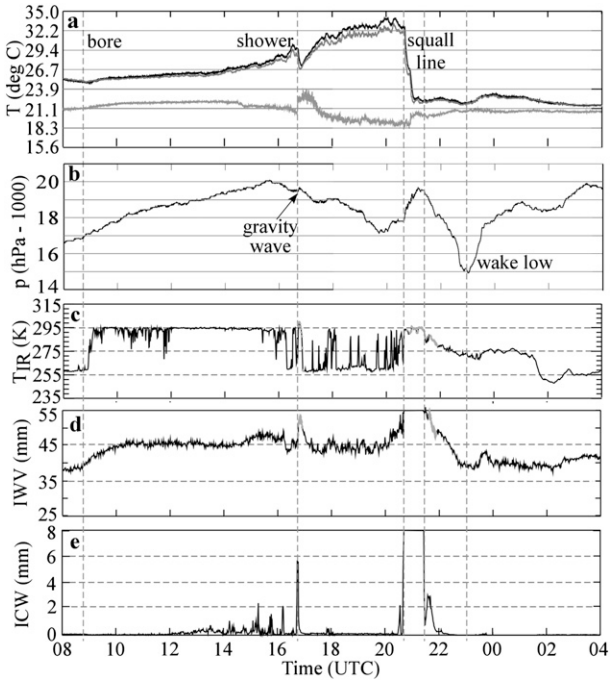

FIG. 14. Time series of surface data (derived from independent surface instrumentation) and radiometer data from the 8 Jun 2007 squall-line case. Surface parameters include (a) T and T_d and (b) pressure (reduced to sea level). MWRP parameters include (c) T_{IR}, (d) IWV, and (e) ICW. The vertical dashed lines refer to significant features that are annotated in (a) and (b).

changes that occur on very short time scales of O(1–10 min), far too short to be sampled by in situ radiosondes.

b. Quantitative precipitation forecasting

MWRP observations around boundaries and large eddies within the convective boundary layer reveal that water vapor exhibits appreciable temporal/spatial variability, and is often enhanced within boundaries via vertical advection within updrafts (Karan 2007). Since convective initiation (CI) is highly sensitive to relatively subtle changes in low-level r_v (Crook 1996; Weckwerth 2000), the MWRP shows considerable potential in improving quantitative precipitation forecasting (QPF) when radiometer data are assimilated into models (Ducroqc et al. 2002; Wulfmeyer et al. 2006).

c. Thermodynamics within clouds and precipitation

The MWRP measurements show a potential for profiling temperature, and hence buoyancy, within precipitating cloud systems. Currently, no other ground-based remote sensing technique is able to routinely probe the temperature within (precipitating) cloud systems up to midtropospheric levels. A more robust passive microwave retrieval scheme could, in principle, utilize information from profiling radars that sample

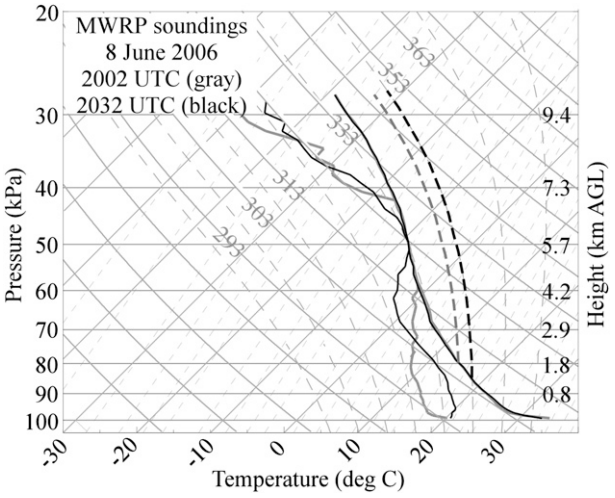

FIG. 15. MWRP soundings, plotted on a skew T–log$p$ diagram. These soundings were sampled just in advance of the squall line and illustrate the rapid destabilization produced by an increase in low-level mixing ratio. Dashed lines represent saturated adiabats based on the lowest 50-mb average values of θ and mixing ratio for each sounding.

Doppler spectra, from which precipitation size distributions can be estimated (e.g., Williams et al. 2007).

d. Boundary layer processes

Because the MWRP can continuously monitor the atmospheric boundary layer, rapid local changes in nocturnal boundary layer (NBL) phenomena can be monitored (e.g., Güldner and Spänkuch 2001). For example, NBL thermodynamic structures often exhibit very large vertical gradients in θ and r_v near the surface. Since the MWRP resolution scales with height, such large gradients are often resolved quite well. For

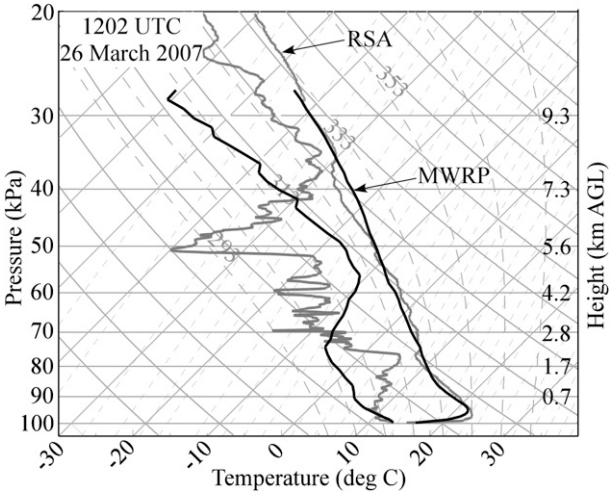

FIG. 16. Nocturnal inversion soundings from the MWRP and RSA radiosonde at 1202 UTC 26 Mar 2007.

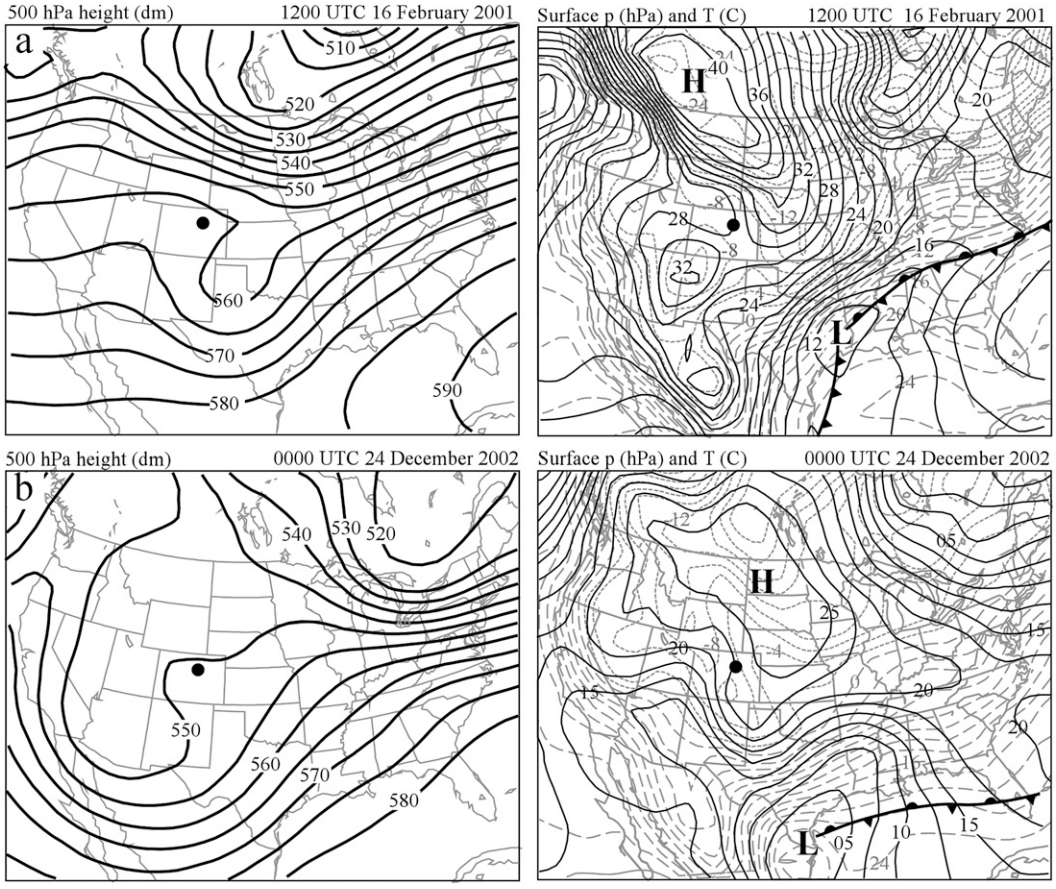

FIG. A1. Analyses of (left) 500-hPa height and (right) surface p and T for each case considered in section 3. In the left, heights of the 500-hPa geopotential surface are contoured every 5 dam (50 m). In the right, isobars of mean sea level p are solid black (contoured every 2 hPa), and isotherms are gray dashed lines (contoured every 2°C). Fronts are represented with the usual symbols. The large dot indicates the location of the MWRP in (a),(b) Boulder or (c)–(e) Huntsville.

example, Fig. 16 shows a good agreement between the MWRP and RSA soundings for a strong nocturnal inversion in Huntsville. In addition, rapid variations in r_v within the ABL (e.g., section 3e) can be related to ABL kinematics when MWRP data are merged with Doppler wind profiler and/or Doppler wind lidar data.

e. Severe storms forecasting

Static stability, usually expressed in bulk form as the convective available potential energy or convective inhibition (CIN; Colby 1984), is used to anticipate the timing and intensity of deep convection. Rapid local changes in vertical thermodynamic profiles are often produced by boundary layer heating, mesoscale vertical motion, and horizontal temperature advection. Continuous monitoring of thermodynamic indices can therefore provide very timely information on CAPE and CIN (e.g., Fig. 15). This capability has been demonstrated by Feltz and Mecikalski (2002), who utilized the hyperspectral Atmospheric Emitted Radiance Interferometer (AERI) instrument to assess the evolution of CAPE and CIN during the 3 May 1999 tornado outbreak in Oklahoma.

f. Winter weather forecasting

MWRP measurements have also been useful in winter precipitation forecasting, such as examination of the lower-atmospheric temperature–humidity profile to determine the relative probability of rain, freezing rain, and snow. The ability to detect supercooled liquid, as illustrated in section 3a, could contribute to multisensor icing algorithms such as the ''current icing potential'' (CIP; Bernstein et al. 2005). In another example (unpublished), the MWRP provided insights on an unexpected (but significant) sleet event around Huntsville. Although the MWRP T profiles were warmer than 0°C below 2 km AGL, dry conditions in the layer promoted a low wet-bulb temperature ($T_w < 0$°C), and hence

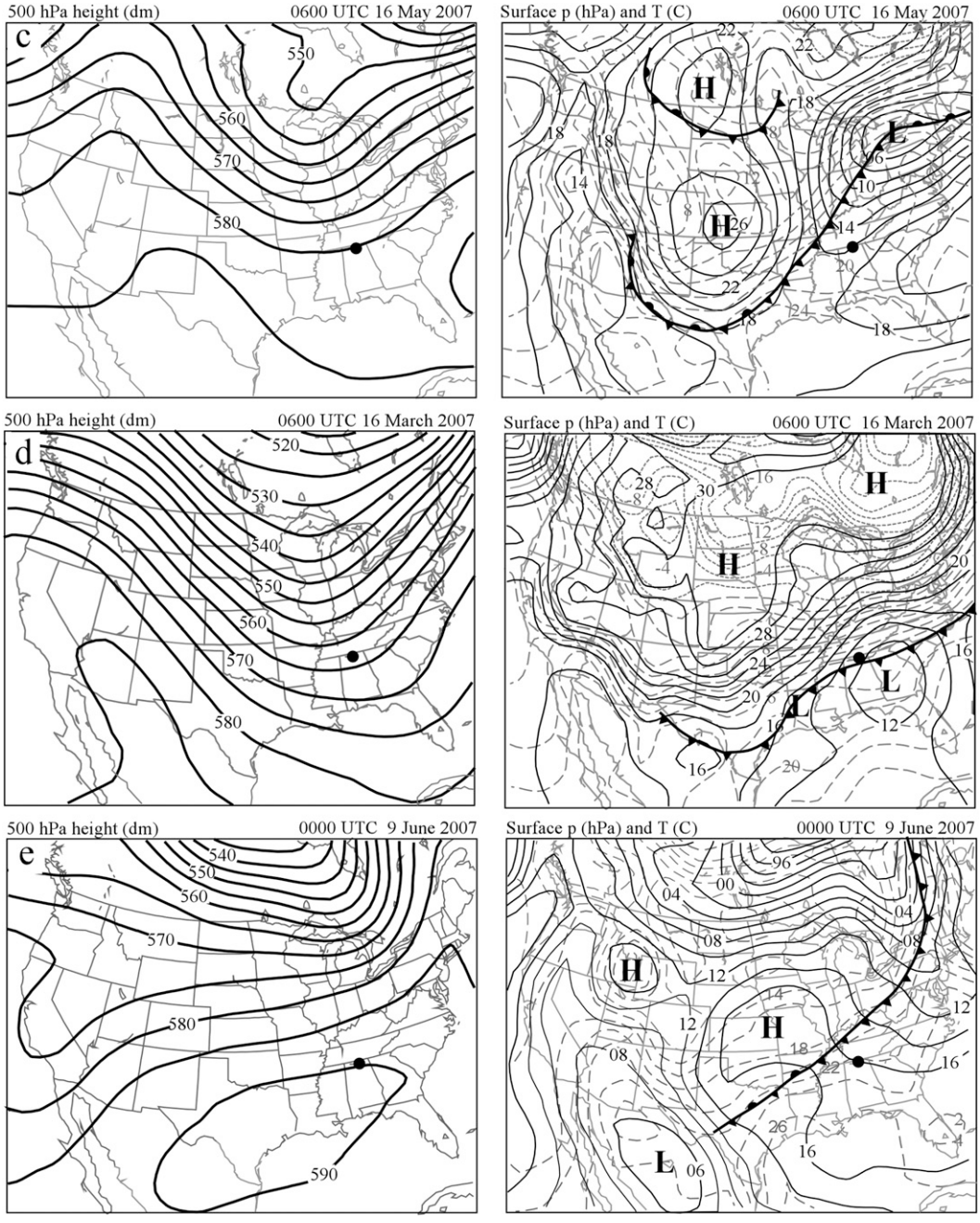

FIG. A1. (*Continued*)

cooling of raindrops and the initiation of raindrop freezing. Integrated measures of temperature, such as thickness, are extensively utilized to forecast winter precipitation type (e.g., Heppner 1992). Radiometric measurements can be used quite effectively to monitor various thickness values (1000–925, 1000–850 hPa) since the integrated temperature measurement errors are likely less than T values at specific heights.

Although the MWRP provides soundings at high temporal resolution, the decreased vertical resolution above 1–2 km does not generally allow the retrieval of large vertical gradients in T and ρ_v that often accompany temperature inversion layers. Recent studies have evaluated the potential improvement in both vertical resolution and accuracy of retrieved thermodynamic profiles using a multisensor approach (e.g.,

wind profilers and profiling radiometers; Bianco et al. 2005).

Assimilation of MWRP data into mesoscale models shows considerable potential to improve the prediction of cloud–mesoscale processes, convective initiation, and precipitation. In this vein, the potential improvements in numerical weather prediction of mesoscale phenomena using a network of collocated MWRPs, wind profilers, and other profiling instrumentation (e.g., ceilometers and vertically pointing precipitation radars) warrants a continued evaluation.

Acknowledgments. Three of the authors (KRK, TC, and DP) acknowledge support from the National Science Foundation under Grants ATM-0079829 (used to procure the UAH MWRP in 2001) and ATM-0533596. One of the authors (RW) acknowledges support from U.S. Army Research Laboratory Contract DAAD17-01-C-0045 (E. Measure, Program Manager).

APPENDIX

Synoptic Analyses

Figure A1 presents surface and 500-hPa analyses for each case discussed in section 3. These are derived from the National Centers for Environmental Prediction (NCEP) and National Center for Atmospheric Research (NCEP–NCAR) reanalysis available on the National Oceanic and Atmospheric Administration Web site. Refer to Kalnay et al. (1996) for details. The analysis times (available at 3-h intervals) presented here are the closest to each event.

REFERENCES

Bernstein, B. C., F. McDonough, M. K. Politovich, B. G. Brown, T. P. Ratvasky, D. R. Miller, C. A. Wolff, and G. Cunning, 2005: Current icing potential: Algorithm description and comparison with aircraft observations. *J. Appl. Meteor.,* **44,** 969–986.

Bianco, L., D. Cimini, F. S. Marzano, and R. Ware, 2005: Combining microwave radiometer and wind profiler radar measurements for high-resolution atmospheric humidity profiling. *J. Atmos. Oceanic Technol.,* **22,** 949–965.

Chahine, M. T., and Coauthors, 2006: AIRS: Improving weather forecasting and providing new data on greenhouse gases. *Bull. Amer. Meteor. Soc.,* **87,** 911–926.

Cimini, D., T. Hewison, L. Martin, J. Gueldner, C. Gaffard, and F. Marzano, 2006: Temperature and humidity profile retrievals from ground-based microwave radiometers during TUC. *Meteor. Z.,* **15,** 45–56, doi:10.1127/0941-2948/2006/0099.

Clarke, R., R. Smith, and D. Reid, 1981: The Morning Glory of the Gulf of Carpentaria: An atmospheric undular bore. *Mon. Wea. Rev.,* **109,** 1726–1750.

Colby, F. P., 1984: Convective inhibition as a predictor of convection during AVE-SESAME II. *Mon. Wea. Rev.,* **112,** 2239–2252.

Crook, N. A., 1996: Sensitivity of moist convection forced by boundary layer processes to low-level thermodynamic fields. *Mon. Wea. Rev.,* **124,** 1767–1785.

Ducroqc, V., D. Ricard, J.-P. Lafore, and F. Orain, 2002: Storm-scale numerical rainfall prediction for five precipitating events over France: On the importance of the initial humidity field. *Wea. Forecasting,* **17,** 1236–1256.

Feltz, W. F., and J. R. Mecikalski, 2002: Monitoring high-temporal-resolution convective stability indices using the ground-based Atmospheric Emitted Radiance Interferometer (AERI) during the 3 May 1999 Oklahoma Kansas tornado outbreak. *Wea. Forecasting,* **17,** 445–455.

——, W. L. Smith, H. B. Howell, R. O. Knuteson, H. Woolf, and H. E. Revercomb, 2003: Near-continuous profiling of temperature, moisture, and atmospheric stability using the Atmospheric Emitted Radiance Interferometer (AERI). *J. Appl. Meteor.,* **42,** 584–597.

Gerber, H., G. Frick, and A. R. Rodi, 1999: Ground-based FSSP and PVM measurements of liquid water content. *J. Atmos. Oceanic Technol.,* **16,** 1143–1149.

Gossard, E. E., S. Gutman, B. B. Stankov, and D. E. Wolf, 1999: Profiles of radio refractive index and humidity derived from radar wind profilers and the Global Position System. *Radio Sci.,* **34,** 371–383.

Güldner, J., and D. Spänkuch, 2001: Remote sensing of the thermodynamic state of the atmospheric boundary layer by ground-based microwave radiometry. *J. Atmos. Oceanic Technol.,* **18,** 925–933.

Haertel, P. T., and R. H. Johnson, 2000: The linear dynamics of squall line mesohighs and wake lows. *J. Atmos. Sci.,* **57,** 93–107.

Han, Y., and E. R. Westwater, 1995: Remote sensing of tropospheric water vapor and cloud liquid water by integrated ground-based sensors. *J. Atmos. Oceanic Technol.,* **12,** 1050–1059.

Heppner, P. O., 1992: Snow versus rain: Looking beyond the ''magic'' numbers. *Wea. Forecasting,* **7,** 683–691.

Herzegh, P. H., S. Landolt, and T. Schneider, 2003: The structure, evolution and cloud processes of a Colorado upslope storm as shown by profiling radiometer, radar and tower data. *Proc. 31st Int. Conf. on Radar Meteorology*, Seattle, WA, Amer. Meteor. Soc., 13.5. [Available online at http://ams.confex.com/ams/pdfpapers/64469.pdf.]

Hogg, D. C., and Coauthors, 1983a: An automatic profiler of the temperature, wind and humidity in the troposphere. *J. Climate Appl. Meteor.,* **22,** 807–831.

——, F. Guiraud, J. Snider, M. Decker, and E. Westwater, 1983b: A steerable dual-channel microwave radiometer for measurement of water vapor and liquid in the troposphere. *J. Climate Appl. Meteor.,* **22,** 789–806.

Ikeda, K., and R. Rasmussen, 2003: Radar observations of a freezing drizzle case in Colorado. *Proc. 31st Int. Conf. on Radar Meteorology*, Seattle, WA, Amer. Meteor. Soc., P5C.1. [Available online at http://ams.confex.com/ams/pdfpapers/64788.pdf.]

Johnson, R. H., 2001: Surface mesohighs and mesolows. *Bull. Amer. Meteor. Soc.,* **82,** 13–31.

Kalnay, E., and Coauthors, 1996: The NCEP/NCAR 40-Year Reanalysis Project. *Bull. Amer. Meteor. Soc.,* **77,** 437–471.

Karan, H., 2007: Thermodynamic and kinematic characteristics of low-level convergence zones observed by the Mobile Integrated Profiling System. Ph.D. dissertation, University of Alabama in Huntsville, 207 pp.

——, and K. Knupp, 2006: Mobile Integrated Profiler System (MIPS) observations of low-level convergent boundaries during IHOP. *Mon. Wea. Rev.,* **134,** 92–112.

Klaus, V., L. Bianco, C. Gaffard, M. Matabuena, and T. Hewison, 2006: Combining UHF radar wind profiler and microwave radiometer for the estimation of atmospheric humidity profiles. *Meteor. Z.,* **15,** 87–97.

Knupp, K., 2006: Observational analysis of a gust front to bore to solitary wave transition within an evolving nocturnal boundary layer. *J. Atmos. Sci.,* **63,** 2016–2035.

Koch, S. E., 2001: Real-time detection of split fronts using mesoscale models and WSR-88D radar products. *Wea. Forecasting,* **16,** 35–55.

——, P. B. Dorian, R. Ferrare, S. Melfi, W. C. Skillman, and D. Whiteman, 1991: Structure of an internal bore and dissipating gravity current as revealed by Raman lidar. *Mon. Wea. Rev.,* **119,** 857–887.

Li, L., J. Vivekanandan, C. H. Chan, and L. Tsang, 1997: Microwave radiometric technique to retrieve vapor, liquid and ice. *IEEE Trans. Geosci. Remote Sens.,* **35,** 224–236.

Liljegren, J. C., B. M. Lesht, S. Kato, and E. Clothiaux, 2001: Initial evaluation of profiles of temperature, water vapor and cloud liquid water from a new microwave profiling radiometer. *Proc. 11th Symp. on Meteorological Observations and Instrumentation,* Albuquerque, NM, Amer. Meteor. Soc., 8.6.

——, S. A. Boukabara, K. Cady-Pereiria, and S. A. Clough, 2005: The effect of the half-width of the 22-GHz water vapor line on retrievals of temperature and water vapor profiles with a twelve-channel microwave radiometer. *IEEE Trans. Geosci. Remote Sens.,* **43,** 1102–1108.

Locatelli, J. D., R. D. Schwartz, M. T. Stoelinga, and P. V. Hobbs, 2002: Norwegian-type and cold front aloft–type cyclones east of the Rocky Mountains. *Wea. Forecasting,* **17,** 66–82.

Loehrer, S. M., and R. H. Johnson, 1995: Surface pressure and precipitation life cycle characteristics of PRE-STORM mesoscale convective systems. *Mon. Wea. Rev.,* **123,** 600–621.

Löhnert, U., S. Crewell, and C. Simmer, 2004: An integrated approach toward retrieving physically consistent profiles of temperature, humidity, and cloud liquid water. *J. Appl. Meteor.,* **43,** 1295–1307.

Marzano, F., D. Cimini, and R. Ware, 2005: Monitoring of rainfall by ground-based passive microwave systems: Models, measurements and applications. *Adv. Geosci.,* **2,** 259–265.

Nehrkorn, T., and C. Grassotti, 2003: Mesoscale variational assimilation of profiling radiometer data. *Proc. 20th Conf. on Weather Analysis and Forecasting/16th Conf. on Numerical Weather Prediction*, Seattle, WA, Amer. Meteor. Soc., P1.12. [Available online at http://ams.confex.com/ams/pdfpapers/70025.pdf.]

Schroeder, J., and E. Westwater, 1991: User's guide to WPL microwave radiative transfer software. NOAA Tech. Memo. ERL WPL-213, Silver Spring, MD, 84 pp.

Schultz, D. M., 2005: A review of cold fronts with prefrontal troughs and wind shifts. *Mon. Wea. Rev.,* **133,** 2449–2472.

Simpson, J. E., 1997: *Gravity Currents: In the Environment and the Laboratory.* Cambridge University Press, 244 pp.

Solheim, F., J. Godwin, E. Westwater, Y. Han, S. Keihm, K. Marsh, and R. Ware, 1998: Radiometric profiling of temperature, water vapor, and liquid water using various inversion methods. *Radio Sci.,* **33,** 393–404.

Vandenberghe, F., and R. Ware, 2003: Four-dimensional variational assimilation of ground-based microwave observations during a winter fog event. *Proc. Int. Workshop on GPS Meteorology*, Tsukuba, Japan, Japan Meteorological Agency, 3–05.

Ware, R., R. Carpenter, J. Güldner, J. Liljegren, T. Nehrkorn, F. Solheim, and F. Vandenberghe, 2003: A multichannel radiometric profiler of temperature, humidity, and cloud liquid. *Radio Sci.,* **38,** 8079, doi:10.1029/2002RS002856.

Weckwerth, T. M., 2000: The effect of small-scale moisture variability on thunderstorm initiation. *Mon. Wea. Rev.,* **128,** 4017–4030.

Westwater, E., 1993: Ground-based microwave remote sensing of meteorological variables. *Atmospheric Remote Sensing by Microwave Radiometry*, M. Janssen, Ed., J. Wiley & Sons, 145–213.

——, Y. Han, and F. Solheim, 2000: Resolution and accuracy of a multi-frequency scanning radiometer for temperature profiling. *Microwave Radiometry and Remote Sensing of the Earth's Surface and Atmosphere*, P. Pampaloni and S. Paloscia, Eds., VSP, 129–135.

——, S. Crewell, C. Mätzler, and D. Cimini, 2005: Principles of surface-based microwave and millimeter wave radiometric remote sensing of the troposphere. *Quat. Soc. Ital. Elettromagn.,* **1,** 50–90.

Williams, C. R., A. B. White, K. S. Gage, and F. M. Ralph, 2007: Vertical structure of precipitation and related microphysics observed by NOAA profilers and TRMM during NAME 2004. *J. Climate,* **20,** 1693–1712.

Wulfmeyer, V., H. S. Bauer, M. Grzeschik, A. Behrendt, F. Vandenberghe, E. V. Browell, S. Ismail, and R. A. Ferrare, 2006: Four-dimensional variational assimilation of water vapor differential absorption lidar data: The first case study within IHOP_2002. *Mon. Wea. Rev.,* **134,** 209–230.

Zhou, D. K., W. L. Smith, X. Liu, A. M. Larar, S. A. Mango, and H. L. Huang, 2007: Physically retrieving cloud and thermodynamic parameters from ultraspectral IR measurements. *J. Atmos. Sci.,* **64,** 969–982.